Experimental and 3D Finite Element Studies of CW Laser Forming of Thin Stainless Steel Sheets

Guofei Chen

Xianfan Xu[1]

School of Mechanical Engineering,
Purdue University,
West Lafayette, IN 47907-1288

Laser forming as a springback-free and noncontact forming technique has been under active investigation over the last decade. Previous investigations are mainly focused on forming of large and thick workpieces using high power lasers, with less work on precision, micro-scale bending of small and thin sheets. In this work, a 4 W continuous wave argon ion laser is used as the energy source, and the laser beam is focused to a beam diameter of tens of micrometers to induce bending of thin stainless steel sheets. When the laser scanning velocity is above 8 mm/s, bending can be explained by the temperature gradient mechanism, while decreasing the scanning velocity leads to the buckling mechanism of bending. The bending angle is measured at various processing conditions. A fully 3D finite element analysis is performed to simulate the thermo-elasto-plastic deformation process during laser forming. Experimental measurements and computational results agree in trend, and reasons for the deviation are discussed. [DOI: 10.1115/1.1347036]

1 Introduction

Laser forming as a springback-free and noncontact forming technique has been under active investigation over the last decade. Instead of applying external forces with forming tools, laser forming is achieved by plastic deformation induced by thermal stresses resulted from rapid laser heating and cooling [1,2]. A schematic of the laser forming process is shown in Fig. 1(*a*). A focused laser beam irradiates the target surface and moves with a scanning velocity along a path called the ''bending edge.'' After the laser beam passes the target and the temperatures of the target return to ambient temperature, a permanent bending angle will be developed as shown in Fig. 1(*b*). The bending mechanisms are determined by the transient temperature field, which in turn is influenced by the thickness and thermophysical properties of the workpiece, the scanning velocity of the laser beam, the laser beam path, the laser power, etc. Three laser bending mechanisms have been discussed in the literature: the temperature gradient mechanism, the buckling mechanism, and the upsetting mechanism [3,4].

Previous investigations on laser forming are mainly implemented using high power lasers on large and thick workpieces [5–7], with less work on the bending behavior of thin sheets using low power lasers [8,9]. Low power laser forming is ideal for applications in microelectronics where high accuracy in bending and curvature modification is needed. For example, Chen et al. [1] employed a pulsed laser-based technique to adjust the curvature of a disk head, with precision better than 1 microradian. They also developed a two-dimensional numerical model to simulate heat transfer and deformation processes during laser bending [2]. Other applications of laser forming include adjusting alignments of optical components in CD, DVD, and MEMS devices. As the dimensions of microelectronic and opto-electronic components continue to be reduced, laser-based high precision curvature modification technique will find more applications in their manufacturing processes.

The goal of this work is to better understand the laser forming process through experimental and numerical studies. It is necessary to establish a 3D numerical procedure since temperature and stress developments in the laser forming process as shown in Fig. 1 are three-dimensional. In this paper, a fully 3D finite element model is developed to simulate the laser forming process. Bending of a thin stainless steel sheet is investigated experimentally using a 4 W continuous wave (CW) argon ion laser. Localized, precision bending is obtained by focusing the laser beam to tens of micrometers to produce localized stress and strain. The bending angle is measured at different laser power, laser scanning velocity, and beam diameter. Computational results are compared with ex-

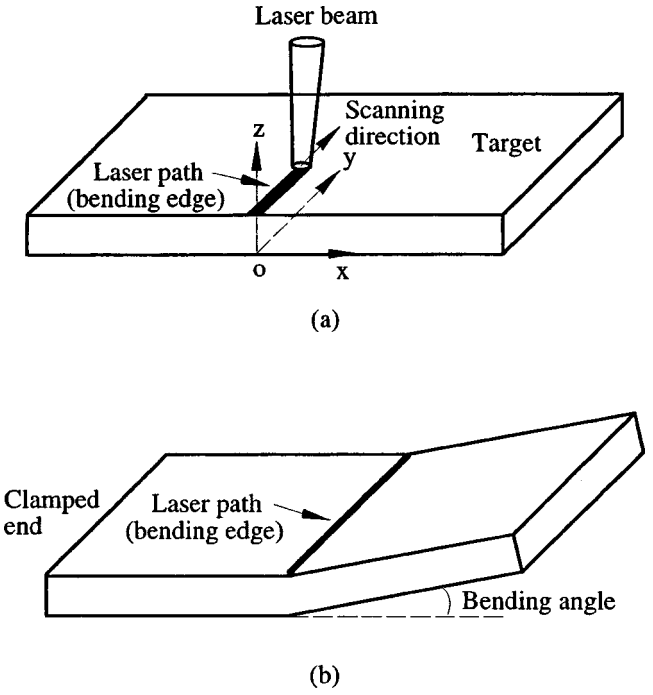

Fig. 1 Schematic of the laser bending process (*a*) during heating (*b*) development of bending angle after cooling

[1]To whom correspondence should be addressed

Contributed by the Manufacturing Engineering Division for publication in the JOURNAL OF MANUFACTURING SCIENCE AND ENGINEERING. Manuscript received June 1999; revised April 2000. Associate Editor: R. Smelser.

perimental measurements. Note that although an argon ion laser is used, results of this work can be extended to other types of lasers, such as the newly available diode pumped solid state lasers which are more compact and easier to be integrated into manufacturing processes.

2 Experimental

Figure 2 illustrates the experimental set-up for CW laser bending as well as for measuring the bending angle. The laser used is a 4 W CW argon ion laser (Lexel Corporation, Model 95) with multiple wavelengths at 488.0 nm (20 percent of total power), 514.5 nm (43 percent of total power), etc. The laser beam is expanded by two lenses and focused onto the target using a focusing lens. The laser beam diameter on the target surface varies from 40 to 120 μm. To avoid melting, the laser power needs to be kept below 2 W and the scanning velocity higher than 8 mm/sec. One end of the target is clamped. A mirror is mounted on a rotating motor, which scans the laser beam over the target surface in the *y*-direction (the direction perpendicular to the paper). Bending is mainly achieved around the *y*-axis into the *z*-direction (Fig. 1(*b*)).

A He-Ne laser is used to measure the bending angle in the *z*-direction. The He-Ne laser beam is focused at the free end of the specimen. The reflected He-Ne laser beam is received by a position sensitive detector with a position sensitivity of 1 μm. When the distance between the position sensor and the specimen is long enough, a small movement at the free end of the specimen produces a measurable displacement of the laser beam at the position sensor. The position change of the He-Ne laser beam at the position sensor can be converted to the bending angle of the specimen using straight-forward geometrical calculations. Using a 0.2 m distance between the position sensor and the specimen, the sensitivity of the bending angle measurement is about 2.5 μrad. The whole apparatus is set on an optical table to isolate vibration.

For most of the experiments in the work, the target is allowed to cool by free convection and radiation. The influence of forced convection cooling on the obtained bending angle is investigated with the use of a 99.99 percent pure nitrogen gas jet. The output gas pressure is 4×10^4 Pa (6.0 psi) and the gas blows in the direction parallel to the target surface. Bending angles obtained with and without using the gas jet are measured and compared.

The specimen used is full-hard 301 stainless steel. The laser and specimen parameters are summarized in Table 1.

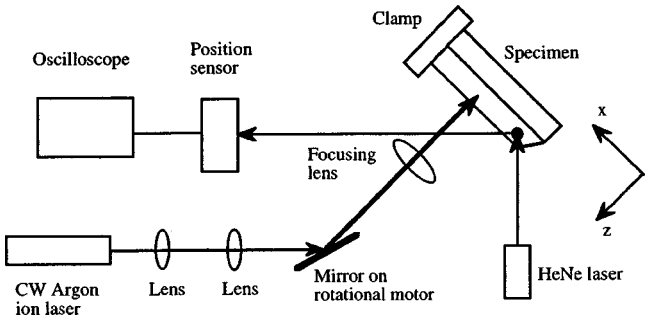

Fig. 2 Experimental setup

Table 1 Laser and specimen parameters used in experiments and finite element analysis

Laser power (W)	1.0 ~ 2.0
Laser scanning velocity (mm/sec)	8.0 ~ 33.5
Laser beam diameter (μm)	40.0 ~ 120.0
Specimen length (mm)	10.0
Specimen width (mm)	1.0
specimen thickness (μm)	100.0

3 Numerical Simulation

Bending induced by the temperature gradient mechanism is simulated in this work. When the duration of laser heating is relatively short, a sharp temperature gradient is produced near the surface, inducing compressive plastic deformation since the thermal expansion of the heated area is constrained by the cooler material that surrounds it. During cooling, tensile stresses arise in the plastically compressed zone due to the bulk constraint of the material contraction. However, the compressive plastic strain is not completely canceled out because heat flows into the adjacent zone and the yield strength increases with decreasing temperature. Therefore, after cooling, the heated surface layer is shrunk, causing the workpiece to bend toward the laser beam. Since bending is obtained due to the nonuniform temperature distribution (the temperature gradient) through the thickness, the bending mechanism is termed the temperature gradient mechanism. In most experiments conducted in this work, the heating period is short and a temperature gradient exists. This will be shown later by the numerical results.

The above description indicates that bending is caused by the plastic deformation induced by thermal stresses and temperature-dependent materials properties, and is strongly dependent on the transient temperature field. The CW laser bending process shown in Fig. 1 causes 3-dimensional temperature and stress fields, therefore, 3D modeling is necessary to compute laser-induced bending. In this work, a 3D finite element analysis is applied to simulate the CW laser bending process induced by the temperature gradient mechanism. The nonlinear finite element solver, ABAQUS (HKS, Inc., Pawtucket, RI), is employed to investigate both the thermal and the mechanical parts of the process.

3.1 Mesh Generation. The computational domain is the same as the dimension of the steel sheet used in the experiments, i.e., 10 mm×1 mm×0.1 mm. Because of the high temperature and stress gradients around the laser path, a dense mesh is necessary there. In order to limit the total number of elements in the simulation, a coarse mesh is used outside the primary processing region, and transition elements in appropriate locations are created to connect the dense mesh and the coarse mesh, as shown in Fig. 3(*a*) and Fig. 3(*b*). The Cartesian coordinate system is attached to the computational domain as shown in Fig. 3(*b*). The center of laser beam moves along the *y*-axis at $x=0$.

Eight-node linear brick elements are used. As shown in Fig. 3(*b*), a fine mesh of elements is placed under the laser irradiated surface, with a length of 120 μm from the center-plane in the *x*-direction. The total element number in this region (Region I) is (in *x*, *y*, *z*): 2×[8×99×9]. In the laser path direction (*y*-direction), the mesh is uniform and the element size is 10 μm in order to accurately capture the flux distribution of the moving laser beam. In the *x* and *z*-directions, the element sizes are increased by stretching. From the dense mesh outwards, the meshes are (in *x*, *y*, *z*): a transition *xz* mesh pattern blended with the reduced number of grids in the *z*-direction in Region II: 2×[1×99×12]; a coarser mesh in Region III: 2×[1×99×3]; a transition *xy* mesh pattern blended with a reduced number of grids in the *y*-direction in Region IV: 2×[1×132×3], and a coarsest mesh in Region V: 2×[14×33×3]. The total element number is 20,790.

A mesh refinement test was performed. If 16 nodes instead of 10 nodes are used in the thickness direction, the temperature field and history are almost not affected, with the maximum temperature difference less than 5 K. Decreasing the element length in the *y*-direction from 10 μm to 6 μm, the maximum temperature dif-

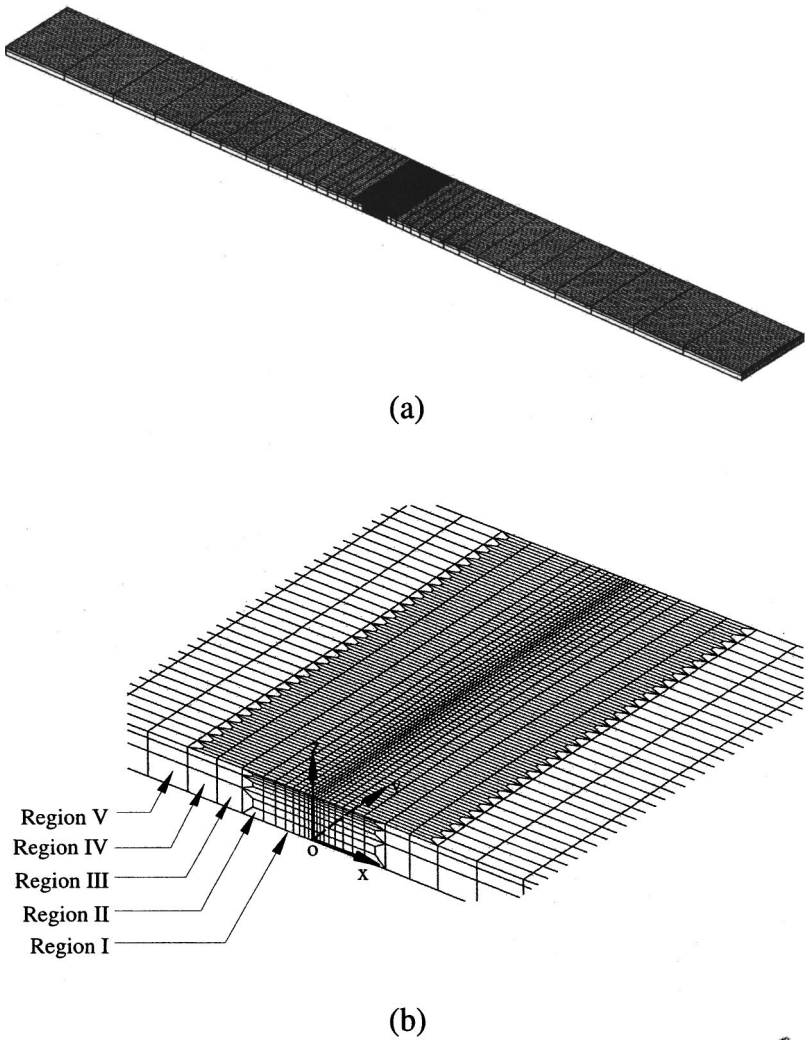

Fig. 3 Mesh for the 3D simulation of laser bending process: (*a*) the total mesh (*b*) the dense mesh around the laser path and the transition mesh pattern

ference is less than 10 K. No change in the subsequent thermo-mechanical stress analysis is caused by these temperature differences.

3.2 Thermal Analysis. Compared with the high laser energy involved in the process, dissipation of energy by plastic deformation is negligible. Therefore, the mechanical calculation can be decoupled from the thermal calculation. The thermal problem is solved first with the 3D heat conduction equation to obtain the temperature field, which is then used as the thermal loading for the mechanical problem. On the other hand, since only small deformation of the target occurs in this work, it is assumed that variations of geometry during the laser bending process have no influence on heat transfer, and the temperature field can be determined on the undeformed mesh. The same mesh is used for both thermal and mechanical calculations.

Laser heating is considered as a volumetric heat source moving at a constant velocity. By assuming the laser flux has a Gaussian distribution, the moving laser flux can be expressed as:

$$I(x,y,t)=I_0 e^{-2(x^2+(y-v_e t-2r_0)^2/r_0^2)} \tag{1}$$

where v_e is the velocity of the scanning laser beam and r_0 is the laser beam radius. The laser flux at the beam center, I_0, can be expressed as:

$$I_0=\frac{2P}{\pi r_0^2} \tag{2}$$

where P is the laser power. In Eq. (1), the term $-2r_0$ is added because the simulation begins when the laser beam is at a distance of $2r_0$ from the sample edge. This is to capture the initial heating of the target by a partial laser beam. Similarly, after the laser beam completely passes the target and reaches the location of $2r_0$ away from the other edge, the laser flux does not irradiate the target anymore and is terminated in the simulation.

The laser flux in the target is:

$$q(x,y,z,t)=(1-R_f)I(x,y,t)e^{-\alpha z} \tag{3}$$

where α is the absorption coefficient of steel. R_f is reflectivity, which is measured to be 0.2 for the oxidized steel surface. Oxidation occurs at the top surface of the workpiece due to the high temperature achieved during laser heating. To better estimate the reflectivity of the steel surface, the reflectivity should be measured *in-situ*, during the heating process. Thus, the oxidation effect and the temperature dependency can all be accounted. However, such measurements are rather involving and the experimental apparatus is not readily available. In the calculation, the measured reflectiv-

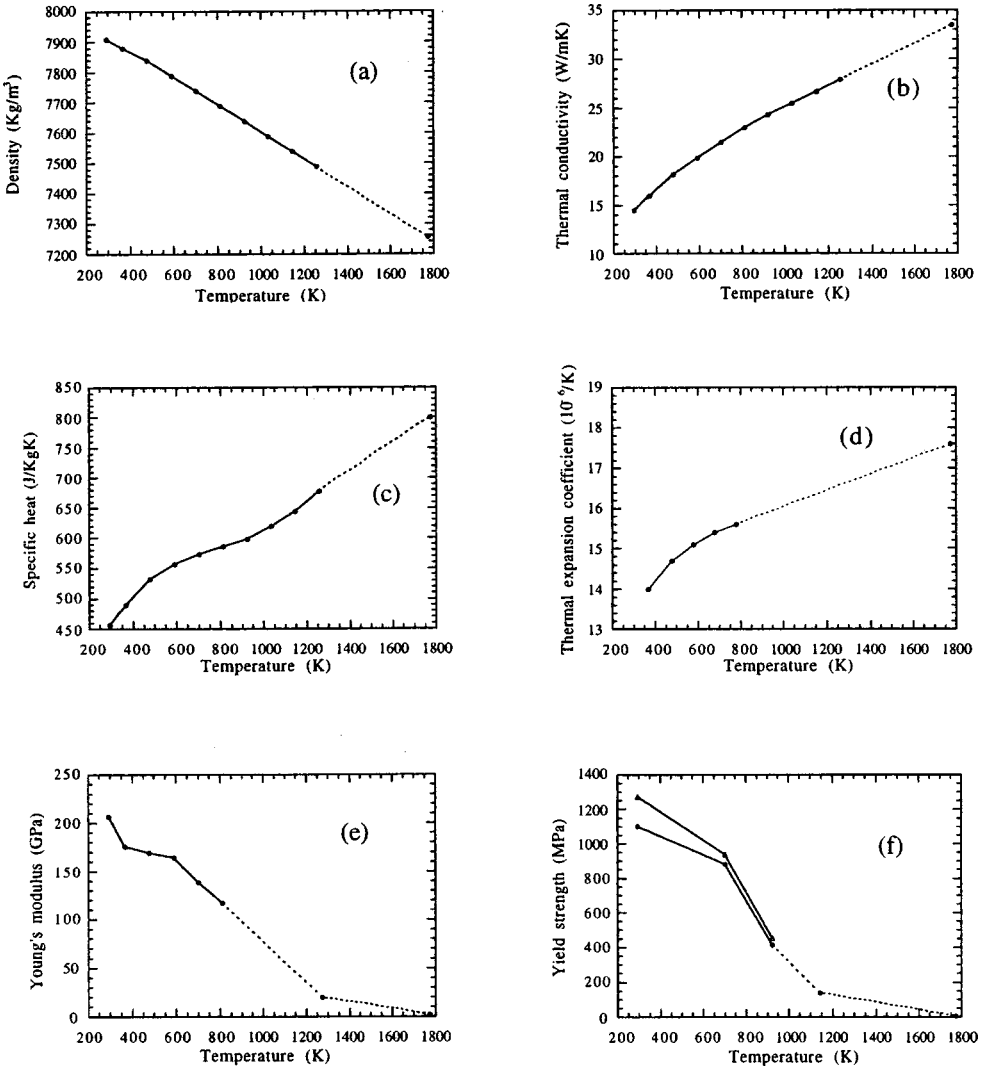

Fig. 4 Thermal and mechanical properties of full-hard 301 stainless steel

ity of the oxidized surface is used since at any instant during scanning, most laser energy is applied to an area that is already raised to a high temperature.

The volumetric distribution of the absorbed laser energy, Q_{ab}, can be expressed as:

$$Q_{ab} = -\frac{dq(x,y,z,t)}{dz} = (1-R_f)\alpha I(x,y,t)e^{-\alpha z} \tag{4}$$

With the laser energy treated as volumetric heat absorption, Q_{ab}, the three-dimensional transient heat conduction equation can be expressed as:

$$\rho c\dot{T} = \nabla\cdot(k\nabla T) + Q_{ab} \tag{5}$$

where the upper dot denotes time derivative. The continuous laser scanning is simulated by a discrete laser source with its center advancing with time. The time step must be small enough so that continuously moving of the laser flux can be accurately approximated. In the calculations, the time step is less than 1×10^{-4} s, during which the laser source moves a distance less than 1 μm, much smaller than the element length of 10 μm in the y-direction. The calculated temperature field is continuous. The time step is controlled according to the criterion that the temperature change between any two adjacent time steps is less than 20 K. No difference is found when 5 K is used. The analysis is proceeded up to the time when the specimen is expected to cool to the room temperature of 300 K. In the analyses, the laser parameters are chosen in such a way that the peak temperature achieved is below the melting temperature of steel, 1670 K. Processes involving melting are not considered in the numerical calculation.

Free convection and radiation boundary conditions are applied to all boundaries, and are expressed as:

$$-k\nabla T\cdot\vec{n} = h(T_s - T_\infty) + \varepsilon\sigma(T_s^4 - T_\infty^4) \tag{6}$$

where $\vec{n}$ is the outward normal at each surface. The convective heat transfer coefficient is taken as 10.0 W/m^{2}K for free convection and an emissivity value of 0.8 is used for calculating the radiative heat flux. Optical reflectivity and emissivity data used are temperature independent since temperature-dependent data are not available in literature, while other thermal properties used are temperature dependent as shown in Fig. 4. The free convective heat transfer coefficient is taken as constant although it varies with temperature. The effect of these assumptions and simplifications on the computation results will be discussed later.

Initially, the temperature of the specimen is at the room temperature:

$$T = T_\infty \tag{7}$$

3.3 Stress Analysis. After the temperature field is obtained, the stress and displacement fields can be calculated as a response

to the thermal loading. Neglecting the dynamic effect, the quasi-static mechanical problem to be solved includes the strain-displacement relations and force equilibrium equations:

$$\varepsilon_{ij}=1/2(u_{i,j}+u_{j,i}) \tag{8a}$$

$$\sigma_{ij,j}+f_i=0 \tag{8b}$$

The incremental plasticity method is employed. The total strain rate is assumed to be the summation of the elastic, plastic and thermal components:

$$\dot{\varepsilon}_{ij}=\dot{\varepsilon}^e_{ij}+\dot{\varepsilon}^p_{ij}+\dot{\varepsilon}^{th}_{ij} \tag{9}$$

Using the von Mises yield criterion and considering the temperature dependency of material properties, the total strain rate can be expressed as [10]:

$$\dot{\varepsilon}_{ij}=\frac{1-2\nu}{3E}\dot{\sigma}_{kk}\delta_{ij}+\frac{\dot{\sigma}'_{ij}}{2G}+\frac{3\sigma'_{ij}}{2\bar{\sigma}H'}\dot{\bar{\sigma}}+\dot{\varepsilon}^{th}\delta_{ij}-\frac{1-2\nu}{3E^2}\dot{E}\sigma_{kk}\delta_{ij}$$
$$-\frac{1}{2G^2}\dot{G}\sigma'_{ij}+\frac{3\sigma'_{ij}}{2\bar{\sigma}H'}\frac{\partial F}{\partial T}\dot{T} \tag{10}$$

where σ'_{ij} is the deviatoric stress tensor, $\bar{\sigma}$ is defined as $\sqrt{3/2}\sqrt{\sigma'_{ij}\sigma'_{ij}}$, H' is defined as $-\partial F/\partial\bar{\varepsilon}^p$, $\bar{\varepsilon}^p=\sqrt{2/3}\sqrt{\varepsilon^p_{ij}\varepsilon^p_{ij}}$, the equivalent strain, and F is the von Mises Yield function.

It is assumed that the steel specimen has a thermo-elasto-plastic behavior with isotropic hardening. Viscous phenomena are neglected because the process is so rapid that high temperatures last shortly in the target. In the laser bending process, the strain rate is high and the yield strength may be strain rate dependent. However, the strain rate dependent yield strength for full-hard (high yield strength) stainless steel is not available. The strain-rate effect is not considered in this analysis. Phase transformation, transformation plasticity and volume change during phase transformation can have a large influence on the stress field in low-alloy steel and mild steel. These effects are not considered in the current simulation for stainless steel 301, which is a high-alloy austenitic steel (18Cr-8Ni) with the martensite start temperature M_s lower than room temperature [11].

The boundary condition is zero displacement at the end of the workpiece that is fully constrained, and the other surfaces are stress free:

$$u_{i,j}=0, \quad \text{at } x=-5\text{ mm} \tag{11a}$$

$$\sigma_{i,j}=0, \quad \text{at } x=5\text{ mm}, \quad y=\pm 0.5\text{ mm},$$
$$z=0, \text{ and } z=0.1\text{ mm} \tag{11b}$$

Initially, it is assumed that the specimen is stress and strain free:

$$\sigma_{i,j}=0, \quad \varepsilon_{i,j}=0 \tag{11c}$$

The validity of assuming zero initial stress and strain will be discussed later. Whenever possible, the materials mechanical properties are considered as temperature-dependent as shown in Fig. 4 [12]. The thermal expansion coefficient for full-hard steel is unknown to the authors, and the data for an extra-hard specimen is used (which is lower than that of full-hard steel). The data given [12] for the Young's modulus and the yield strength are in a certain range, and the averaged values for Young's modulus and the lower bound of the yield strength are used in the calculation. The room temperature value of the Poisson's ratio of 0.3 [12] is used throughout the calculations since the temperature-dependent data are unknown to the authors. Influences of uncertainties of these data have been studied using a numerical uncertainty analysis of two-dimensional pulsed laser bending of steels [2]. It was found that a 10 percent difference in thermal expansion coefficient changes the bending angle by about 10 percent, while the uncertainties in other thermophysical properties and in extrapolations to high temperatures (shown in Fig. 4 as the dashed lines) yielded results within a few percent.

4 Results and Discussions

The result of a benchmark case is presented first to provide the general trends of temperature, stress and strain development. Then, bending angles calculated with different laser parameters are presented and compared with the measured data.

4.1 Numerical Results of a Benchmark Case. A benchmark case with laser power of 2 W, beam diameter of 80 μm and scanning velocity of 8.0 mm/s is simulated to show the transient temperature, stress, strain and displacement development. The temperature distributions on the top and bottom surfaces along the line $x=0$ are shown in Figs. 5(*a*) and 5(*b*). When the laser beam starts to irradiate from one edge ($y=0$) and moves forward, the temperature at the other edge ($y=1$ mm) increases before the laser beam arrives because of heat diffusion. At the beginning of laser heating, the peak temperatures on the top and bottom surfaces increase gradually as shown by the peak temperatures from 0.03 s to 0.096 s in Figs. 5(*a*) and 5(*b*). When the laser beam moves closer to the other edge and just before the laser beam leaves the target at 0.128 s, the peak temperatures at both the top and the bottom surfaces rise quickly as can be seen by comparing the peak temperatures at $t=0.096$ s and $t=0.128$ s. This is be-

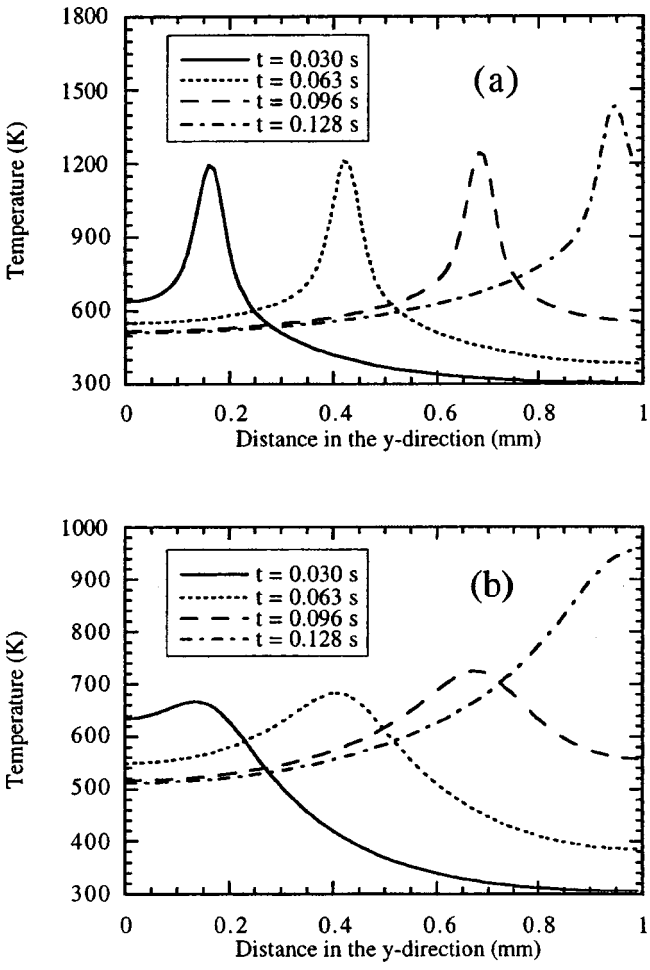

Fig. 5 Temperature distributions along the *y*-direction at $x=0$ at different times (*a*) at the top surface (*b*) at the bottom surface

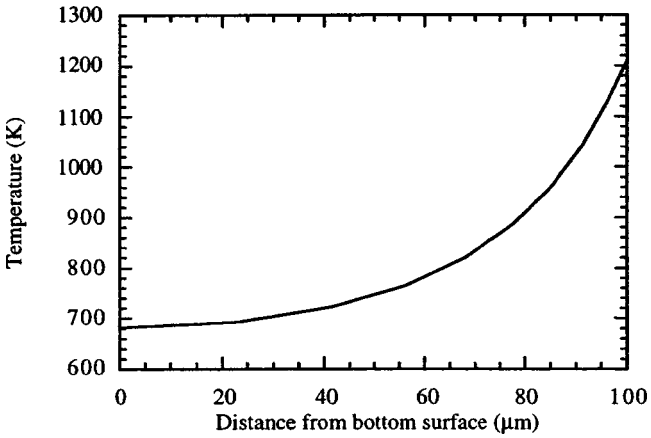

Fig. 6 Temperature distribution along the *z*-direction underneath the laser beam center ($x=0$ mm, $y=0.42$ mm, $t=0.063$ s)

cause the boundary at $y=1$ mm restricts the laser heat flux from being dissipated and thus accelerates the temperature increase in the target.

Figure 6 shows the temperature distribution along the *z*-direction underneath the laser beam center at $t=0.063$ s, which is at $x=0$ mm, $y=0.42$ mm. The temperature gradient decreases gradually from the top to bottom surfaces. The temperature gradient near the heated surface is as high as 2.2×10^7 K/m. A large temperature difference exists between the top and the bottom surface, varying from 1200 K to less than 700 K. Therefore, the temperature gradient mechanism is the bending mechanism.

The developments of stresses σ_{xx} and σ_{yy} at the surface along the beam path ($x=0$) are shown in Figs. 7(*a*) and 7(*b*), respectively. The circles on the curves indicate the locations of the center of the laser beam. At time instants of 0.063 s and 0.096 s, compressive stresses are developed in the regions right ahead of the laser source, which is in the heating period; while tensile stresses are presented in the regions behind the laser source, which is in the cooling period. After the workpiece cools down completely to the ambient temperature, residual stresses along the entire laser path are tensile, while compressive residual plastic strains are distributed at the surface of the workpiece along the laser path at $x=0$ as shown in Fig. 8. The compressive residual plastic strains cause shrinkage in the laser irradiated area and lead to bending of the workpiece.

The residual stress distribution at the surface of the workpiece along the line $y=0.5$ mm is shown in Fig. 9. Very high tensile stresses are generated narrowly around the laser path.

Deformation of the workpiece during laser heating is illustrated in Fig. 10, which shows the displacement u_z along three lines at $y=0.12$, 0.69, and 0.90 mm at $t=0.096$ s. At this time instant, the laser beam center is at $y=0.69$ mm, the temperature at $y=0.12$ mm is increasing, and the temperatures at $y=0.69$ and 0.90 mm are decreasing. The peak temperature is located at $y=0.69$ mm. From Fig. 10, it can be seen that a bump is formed at $y=0.69$ mm because the center of the laser beam is located there at that time instant, and the thermal expansion is the greatest. The target deformation occurs in the region 0.5 mm from the center of the laser beam ($x=0$), with convex curvatures along $y=0.69$ mm and $y=0.90$ mm, and a concave curvature along $y=0.12$ mm. Outside the central region ($x>0.5$ mm), the displacements along the above three lines are the same. As shown in Fig. 10, the same amount of displacement occurs at $x=5$ mm.

The history of the displacement u_z at the center of free end ($x=5$ mm, $y=0.5$ mm) is shown in Fig. 11. Bending is away from the laser beam at first, then reverses its direction at $t=0.085$ s. Bending is towards the laser beam after the workpiece has cooled

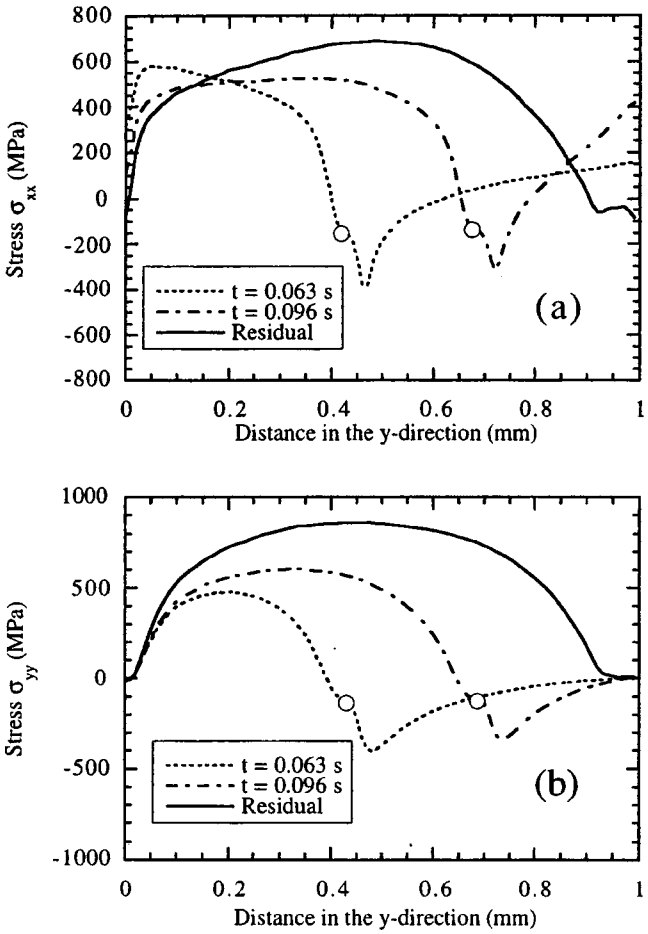

Fig. 7 Stress distribution at the top surface along the line $x=0$ (*a*) σ_{xx}, (*b*) σ_{yy}

down. Although the laser passes the target in 0.14 s, the deformation process ends at 0.16 s in the *z*-direction due to the slow cooling process.

In the above calculations, the heat transfer coefficient of free convection and emissivity are taken to be 10 W/m^{2}K and 0.8, respectively. If 1000 W/m^{2}K is used instead of 10 W/m^{2}K for the convection heat transfer coefficient, the peak temperature decreases by less than 40 K. Note that when the nitrogen gas jet is

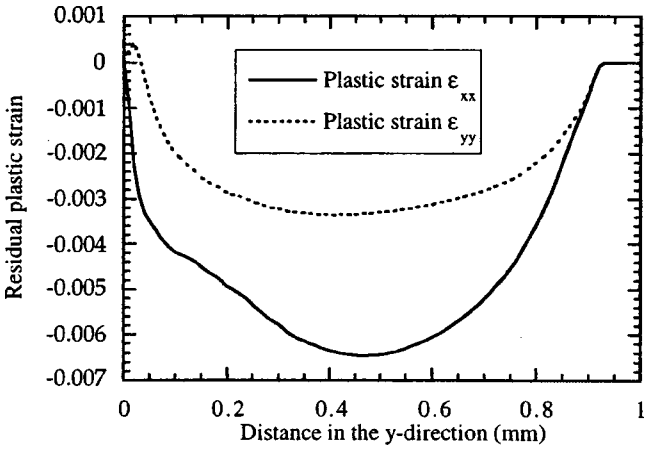

Fig. 8 Residual plastic strain distribution at the top surface along the laser path at $x=0$

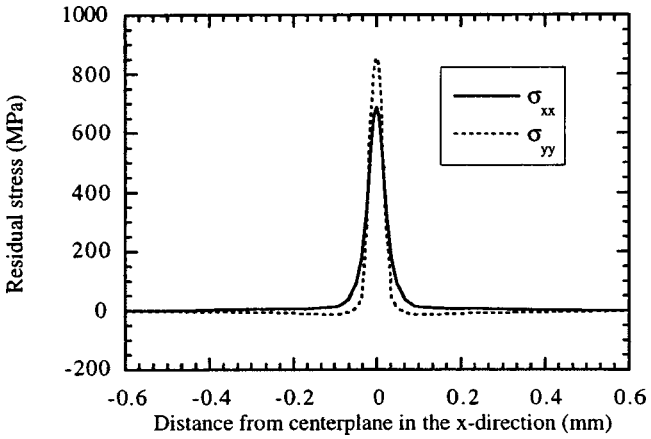

Fig. 9 Residual stress distribution at the top surface along the line $y=0.5$ mm

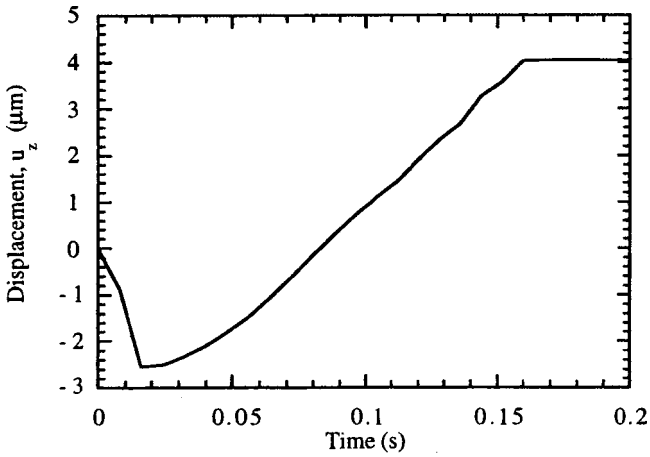

Fig. 11 History of the displacement u_z at the center of the free end

used in the experiment for forced convection cooling, the convective heat transfer coefficient should still be less than 1000 W/m^{2}K. The major temperature difference between the simulations using 10 W/m^{2}K and 1000 W/m^{2}K occurs during cooling after the laser beam passes the specimen. The calculated bending angle decreases by 9 percent when the heat transfer coefficient of convection is increased from 10 W/m^{2}K to 1000 W/m^{2}K. This shows that, assuming a constant free convection coefficient of 10 W/m^{2}K would not cause a significant error in computing the bending angle since the free convection coefficient should be less than tens of W/m^{2}K. Similarly, because of the much smaller radiative flux at the surfaces compared with the laser heat flux, bending results are not sensitive to the emissivity value. The decrease of the bending angle by a large increase in the convection heat transfer coefficient is verified by the experiments. When the gas jet is used, depending on laser parameters, the decrease of the bending angle is between 6 and 10 percent.

4.2 Comparison between Experimental and Numerical Results. Bending angles are measured at different laser powers, beam diameters and scanning velocities. Figure 12(*a*) shows the measured bending angle as a function of laser power at a constant scanning velocity of 8 mm/s and a constant beam diameter of 40 μm. The bending angle increases linearly with the laser power because of the increase of temperature. The error bars in the figure indicate the repeatability of the measurements. When the laser power is higher than 1.5 W, the surface is melted. Figure 12(*b*) shows the measured bending angle as a function of the beam diameter at a constant laser power of 2 W and a constant scanning velocity of 8 mm/s. The bending angle decreases with the increase of the beam diameter because of the decrease of the laser flux which leads to lower temperatures. At a beam diameter of 40 μm, the obtained bending angle is much higher. Melting occurs when the beam diameter is less than 50 μm.

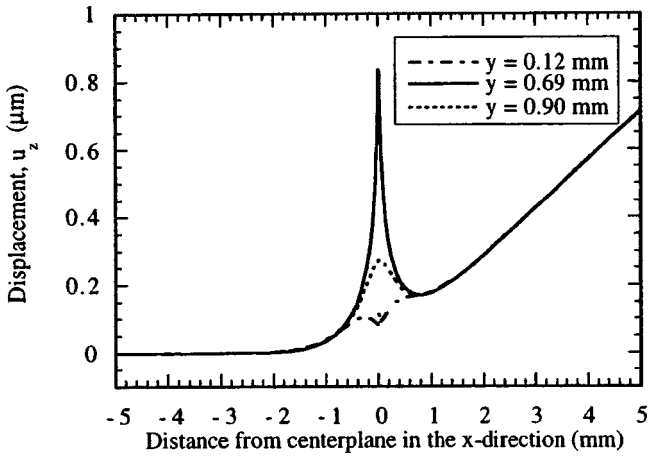

Fig. 10 Displacement (u_z) along the x-axis at $t=0.096$ s

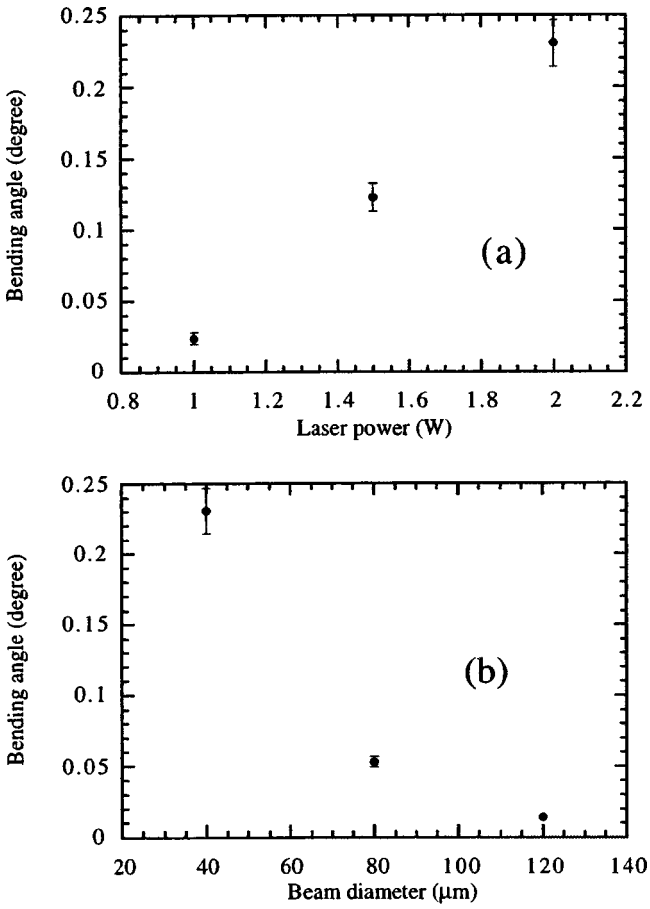

Fig. 12 (*a*) Measured bending angle as a function of laser power at a constant scanning velocity of 8 mm/s and a constant beam diameter of 40 μm (*b*) measured bending angle as a function of the laser beam diameter at a constant laser power of 2 W and a constant scanning velocity of 8 mm/s

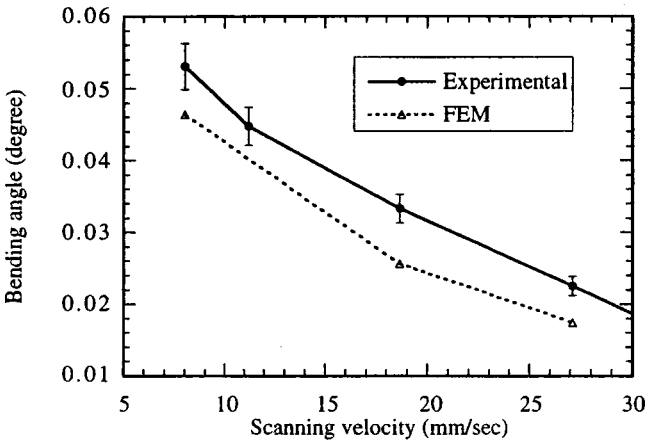

Fig. 13 Measured and calculated bending angles as a function of the scanning velocity at a constant laser power of 2 W and a constant beam diameter of 80 μm

As can be seen from Figs. 12(*a*), (*b*) as long as the peak temperature is kept below the melting point, the repeatability of the obtained bending angle is better than 0.004 deg, indicating that the laser based technique can be used to achieve high precision in bending.

Figure 13 compares measured and calculated bending angles at a laser power of 2 W and a beam diameter of 80 μm, but at different scanning velocities. Increasing the scanning velocity decreases the bending angle because of the decrease of the energy input. The calculated bending angle agrees with the trend of the measured results, but is about 20 percent lower. A number of factors can contribute to the discrepancy between experimental results and simulations, including the temperature dependency of optical reflectivity which is not known and is not considered in the simulations, the use of the thermal expansion coefficient of extra-hard steels, and negligence of initial compressive residual stresses in the target. It has been shown [2] that both neglecting the initial compressive stresses and using the expansion coefficient of extra-hard steel which is smaller than that of the full hard steel would underpredict the bending angle.

With the laser parameters described above, bending is induced by the temperature gradient mechanism. Bending angles are all developed toward the laser beam. If the scanning velocity is reduced, then the buckling mechanism could play a role. The buckling mechanism occurs when the laser scanning velocity is slow and the target is thin, and the heat diffusion length is much larger than the target thickness [13]. Therefore, the region around the laser path is heated almost uniformly in the thickness direction. In this case, similar to a beam under compression, the nearly homogeneously heated section will buckle and the target may be bent either toward or away from the laser beam depending on the pre-curvature of the target and the initial residual stresses. In the experiment, it has been seen that if the scanning velocity is reduced to 0.15 mm/s, the bending direction depends on the pre-curvature of the target: bending is toward the laser beam when the pre-curvature is concave and is away from the laser beam when the pre-curvature is convex. The bending angle is as high as 10 deg for the first laser scan. Additional bending from subsequent laser scans decreases gradually. After about 40 scans, bending by 90 deg is obtained. These phenomena show that bending at a low laser scanning velocity is dominated by the buckling mechanism.

5 Conclusions

Continuous wave laser forming of thin stainless steel sheet was studied. Experimental studies were conducted to find out relations between bending angles and processing parameters, including the laser power, beam diameter and scanning velocity. When the surface of the workpiece was kept below the melting point, the repeatability of the obtained bending angle was better than 0.01 deg. The laser forming process was simulated using a fully 3D finite element model to illustrate the transient temperature, stress, strain and displacement development. The calculated results agreed with the trend of the experimental data. When the laser scanning velocity was high, bending was due to the temperature gradient mechanism, while decreasing the scanning velocity led to bending by the buckling mechanism.

Acknowledgment

Support to this work by the National Science Foundation (DMI-9813758 and DMI-9908176) is gratefully acknowledged.

References

[1] Chen, G., Xu, X., Poon, C. C., and Tam, A. C., 1998, ''Laser-Assisted Microscale Deformation of Stainless Steels and Ceramics,'' Opt. Eng., **37**, No. 10, pp. 2837–2842.

[2] Chen, G., Xu, X., Poon, C. C., and Tam, A. C., 1998, ''Experimental and 2D Numerical Studies on Micro-scale Bending of Stainless Steel with Pulsed Laser,'' *Proceedings of the 1998 ASME International Congress and Exposition*, HTD-Vol. 36-4, pp. 49–57, also to appear in J. Appl. Mech.

[3] Vollertsen, F., 1994, ''Mechanisms and Model for Laser Forming,'' *Laser Assisted Net Shape Engineering, Proceedings of the LANE'94*, Vol. 1, M. Geiger and F. Vollertsen, eds., pp. 345–360.

[4] Geiger, M., and Vollertsen, F., 1993, ''The Mechanisms of Laser Forming,'' CIRP Ann., **42**, pp. 301–304.

[5] Scully, K., 1987, ''Laser Line Heating,'' J. Ship Prod., **3**, pp. 237–246.

[6] Geiger, M., Vollertsen, F., and Deinzer, G., 1993, ''Flexible Straightening of Car Body Shells by Laser Forming,'' SAE paper 930279, pp. 37–44.

[7] Hsiao, Y. C., Shimizu, H., Firth, L., Maher, W., and Masubuchi, K., 1997, ''Finite Element Modeling of Laser Forming,'' *Proceedings of Laser Institute of America, ICALEO '97*, Vol. 83, Part 1, pp. 31–40.

[8] Yau, C. L., Chan, K. C., and Lee, W. B., 1998, ''Laser Bending of Leadframe Materials,'' J. Mater. Process. Technol., **82**, pp. 117–121.

[9] Namba, Y., and Yamaguchi T., 1998, ''Laser Forming of Metals Using Few-watt Nd:YAG Lasers,'' *Conference on Lasers and Electro-Optics Europe-Technical Digest 1998, IEEE*, Piscataway, NJ, USA, p. 8 CMB4.

[10] Chen, G., 1999, *Experimental and Numerical Studies of Micro-scale Laser Bending*, Ph.D. thesis, Purdue University.

[11] Honeycombe, R. W. K., and Bhadeshia, H. K. D. H., 1996, *Steels: Microstructure and Properties*, 2nd Ed., Edward Arnold, a division of Hodder Headline PLC, London, Great Britain.

[12] Maykuth, D. J., 1980, *Structural Alloys Handbook*, Vol. 2, Metals and Ceramics Information Center, Battelle Columbus Laboratory, Columbus, OH, pp. 1–61.

[13] Holzer, S., Arnet, H., and Geiger, M., 1994, ''Physical and Numerical Modeling of the Buckling Mechanism,'' *Laser Assisted Net Shape Engineering, Proceedings of the LANE'94*, Vol. 1, M. Geiger and F. Vollertsen, eds., pp. 379–386.